Geomech. Geophys. Geo-energ. Geo-resour. (2020) 6:65
https://doi.org/10.1007/s40948-020-00192-8

ORIGINAL ARTICLE

The influence of CO_2-transformed iron oxide grain coatings on the frictional stability and transport properties of simulated faults in sandstones

Chaoyi Wang · Derek Elsworth

Received: 6 December 2019 / Accepted: 22 October 2020 / Published online: 27 October 2020
© Springer Nature Switzerland AG 2020

Abstract Carbon sequestration involves long-term containment of CO_2 in ideally sealed reservoirs. However, CO_2 migration can weaken rocks and faults by geochemical alteration, elevate risks of seismic hazards, and loss of inventory. Recent studies show that CO_2 bleaching can alter the iron oxide grain coating of sand-sized quartz in sandstones, which may impose a significant influence on frictional stability and permeability evolution of faults in sandstones. This study investigates the influence of iron oxide grain coatings via coupled shear-flow experiments on uncoated, hematite-coated, and CO_2-transformed goethite-coated synthetic sand gouge. Shear strength, frictional stability, healing/relaxation, and shear-parallel permeability are measured in velocity-stepping and slide-hold-slide loading modes. Hematite-coated sand exhibits the highest shear strength, followed by goethite-coated and uncoated sand. All samples, both coated and uncoated, show similar residual shear strength. Frictional stability measurements suggest hematite-coated sand may undergo potential seismic slip (negative (a − b) values); goethite-coated sand is aseismic (positive (a − b) values) but features higher frictional healing and relaxation. Shear-parallel permeability enhances during initial shear in all samples, followed by a sharp decline after the peak strength, except for goethite-coated sand, for which permeability reduction is moderate. SEM characterizations pre- and post-shear suggest that the competitive liberation, transport, and clogging of coating particles and shear-produced wear products can be an important mechanism in permeability evolution.

Keywords CO_2 alteration · Grain coating · Fault breaching · Fault permeability · Frictional stability

C. Wang (✉) · D. Elsworth
Department of Energy and Mineral Engineering, EMS Energy Institute, and G3 Center, The Pennsylvania State University, University Park, PA, USA
e-mail: wang4214@purdue.edu

Present Address:
C. Wang
Department of Physics and Astronomy, Purdue University, West Lafayette, IN, USA

D. Elsworth
Department of Geosciences, Pennsylvania State University, University Park, PA, USA

1 Article Highlights

- Novel miniaturized double direct shear (DDS) apparatus enables coupled shear-flow experiments.
- Goethite-coated sand features lower friction but higher permeability and rates of relaxation and healing than hematite-coated sand.
- Clogging caused by clustering of coating material and transport of wear products may significantly reduce permeability.

2 Introduction

Geological carbon sequestration injects carbon dioxide (CO_2) into aquifers or reservoirs. It is a promising technology for removing atmospheric CO_2 while replenishing carbon resources in the Earth's subsurface (Benson and Cole 2008). Injecting large volumes of fluid at high rates can disturb the subsurface stress field, creating fractures, reactivating pre-existing fractures and faults, and causing unfavorable consequences of gas breaching, migration, and induced seismicity (Guglielmi et al. 2015; Elsworth et al. 2016; Zoback and Gorelick 2012; Ellsworth 2013). Substantial research efforts have been devoted to study the storage capacity, caprock stability, and seismic risks of CO_2 storage (Fabriol et al. 2010; Fleury et al. 2011; Bader et al. 2014; Rohmer and Seyedi 2010; De Lary et al. 2015). CO_2 is chemically active and can alter the mineralogy of surrounding rocks and faults, inducing mechanical weakening (Wang et al. 2017a; Altman et al. 2014; Rinehart et al. 2016). Migrating CO_2 plumes can cause stress disturbance and alteration in its path (Busch et al. 2014; Busch and Müller 2011). CO_2 bleached sandstone samples retrieved from the outcrop of an analog CO_2 reservoir (near Crystal Geyser, Utah) show significantly lower fracture toughness relative to the unaltered sandstone (Major 2014). Characterization of these samples indicates the presence of hematite as a sand grain coating in the unaltered samples that is presumably transformed to goethite by CO_2 bleaching and may contribute to this weakening. Core samples retrieved from natural analog CO_2 reservoirs from scientific drilling investigations (Busch et al. 2014; Kampman et al. 2014; Kampman 2013) show significant CO_2 brine migration in fault zones, dissolving hematite, carbonate, and gypsum. Laboratory experiments (Hangx et al. 2015; Bakker et al. 2016) using fault gouge made from natural sandstones show that CO_2 brine dissolves diagenetic dolomite cementation. The alteration results in increases in porosity, permeability, and significant mechanical weakening. Frictional behavior of faults in CO_2 reservoirs and caprocks are more likely to slide stably and thus impose reduced seismic risk (Bakker et al. 2016; Samuelson and Spiers 2012).

Iron oxides are the most common products of weathering by geochemical processes, with goethite ($\alpha - FeOOH$) being the most abundant (Schwertmann 2003). Hematite, however, is a more mature and stable iron oxide that can be commonly found in soils and sandstones in regions with higher temperatures and water activities. Geological alteration of hematite to goethite in soils has been previously reported both in nature and in laboratory experiments (Schwertmann 1971), where hematite ($\alpha - Fe_2O_3$) in the soil is dissolved by carbon-rich organic matter and reprecipitated as goethite ($\alpha - FeOOH$). Specifically, the iron in amorphous ferric hydroxide is complexed by carbon-rich organic compounds and inhibited from forming a hematite precipitate but converted to goethite instead. Natural hematite and goethite are poorly crystallized, with small crystalline size ranging from sub-microns to microns; they can typically form Fe^{3+}–O–Si bonds, thus forming an iron oxide coating layer on the sand grains. These iron oxides coatings such as hematite and goethite, serve an important role in characterizing the mechanical properties of the host soils and rocks. For example, one previous study (Cundy and Hopkinson 2005) suggests that precipitation of iron oxides can enhance the undrained shear strength of soils. Since quantifying the influences of iron oxide coating materials is challenging, previous studies intentionally remove iron oxide coatings using strong reductants (Rao et al. 1995). Other studies investigate the effect of iron oxide coatings on the shear strength of sand using lab synthesized hematite and goethite coated sand (Choo et al. 2015; Larrahondo et al. 2011; Larrahondo and Burns 2014). Results indicate that hematite coated sands show the highest shear strength followed by goethite-coated sand then uncoated sand. In addition to shear strength, slip stability and permeability are two crucial factors that influence the potential for seismicity and CO_2 leakage. The potential for this response may be codified through rate and state friction (RSF) laws that describe the frictional evolution and stability of faults during earthquake cycles (Ruina 1983; Dieterich 1978, 1979a, b; Rice et al. 2001; Marone 1998) and the linkage of RSF to the evolution of permeability. For theoretical behavior of rate state friction and its applications to studying the Earth's seismic cycles are discussed abundantly elsewhere (Ruina 1983; Dieterich 1979a, b; Rice et al. 2001; Scholz 1998; Marone 1998). The constitutive relation of RSF can be summarized as:

$$\mu = \mu_0 + a\ln\left(\frac{V}{V_0}\right) + b\ln\left(\frac{V_0\theta}{D_c}\right) \quad (1)$$

$$\frac{d\theta}{dt} = 1 - \frac{V\theta}{D_c} \quad (2)$$

in which, μ and μ_0 are the friction coefficients of the current state and previous steady-state; V and V_0 are the slip velocity of the current and previous steady-state; θ and D_c are the state variable and characteristic slip distance; a and b are the stability parameters, which are characteristic to the system and primarily related to its mineral texture and composition (Ikari et al. 2011; Fang et al. 2018). a and b values can be captured in the laboratory by performing direct shear experiments using a velocity stepping loading mode on rocks and gouge materials (Mair and Marone 1999). The frictional response of a sliding segment of a fault can be derived from a simple system consisting of a sliding block driving by a spring with a certain stiffness. If $(a - b)$ value is greater than zero, the system is theoretically aseismic. Otherwise, the system is prone to seismic rupture, given a sufficiently small driving stiffness.

Risks of seismic fault reactivation and permeability change due to CO_2 bleaching are concerns for carbon migration after sequestration. It is crucial to understand the influencing factors. However, most characterizations of the concurrent evolution of friction and permeability (Fang et al. 2018; Fang et al. 2016; Im et al. 2018; Wang et al. 2017b; Samuelson et al. 2009; Fang et al. 2017; Yasuhara et al. 2006) of sandstones ignore the impacts of grain coatings. We conduct flow-shear laboratory experiments on hematite-, goethite- and un-coated sand to broaden understanding of frictional stability and permeability characteristics of sandstone faults subjected to CO_2 alteration. These experiments are conducted in a novel double direct shear apparatus (Li et al. 2019) within a simple-triaxial pressure vessel and constrained by scanning electron microscope (SEM) imaging and particle size distribution (PSD) analysis.

3 Experimental methods and materials

3.1 Experimental methods

We use a miniature double direct shear (DDS) configuration similar to the macro-scale apparatuses reported previously (Marone 1998; Mair and Marone 1999; Samuelson et al. 2009; Collettini et al. 2009). The validity and fidelity of the apparatus and the experimental method used in this study are discussed in detail elsewhere (Li et al. 2019). The DDS setup is capable of conducting experiments at temperatures of up to 80 °C and confining pressure of up to 25 MPa. Similar to single direct shear methods (Bakker et al. 2016; Samuelson and Spiers 2012; Crawford et al. 2008), DDS is particularly effective in concurrently measuring the evolution of shear strength, slip stability, frictional healing, and relaxation behavior, and more advantageous by minimizing the resistance introduced by the jacketing system, yielding highly resolved measurements. The DDS apparatus in this study incorporates real-time shear-parallel permeability measurements. We present a schematic of the apparatus in Fig. 1a. The sample core configuration comprises three roughened steel platens sandwiching two layers of unconsolidated sand gouges. There are saw-tooth grooves on the platen-gouge interface to prevent interface sliding. Each tooth is an equilateral triangle, the peak-to-peak distance between the saw-teeth are 0.02 in/$\sim$ 500 μm to accommodate at least five sand particles across a single valley (in this study). The confining pressure is the hydrostatic pressure applied by Pump A to the jacketed exterior of the sample, as shown in Fig. 1a. Candidate CO_2 reservoirs are usually located at depths of several kilometers, with temperatures ranging from 50 to 120 °C. However, our current configuration has a limitation against jacket rupture under high temperatures and high confining stresses during shearing. Therefore, all experiments are conducted at room temperature and at a constant confining pressure of 3 MPa to approximate the in-situ condition. During the shear experiments, the top and bottom platens are kept in place while shear stress is applied by driving the center platen towards the support base via the pressure in Pump B. Concurrently, pore fluid (deionized water at room temperature, the water is not de-aired) is injected by Pump C at a constant differential fluid pressure of 35 kPa. The constant differential fluid pressure is chosen to avoid the mobilization of sand particles and optimize the test time due to the limited pump reservoir volume ($\sim$ 500 ml). The maximum flow rate in all of our experiments does not exceed 15 ml/min. The downstream is directly connected to the atmosphere. Pressures and flow rates are monitored

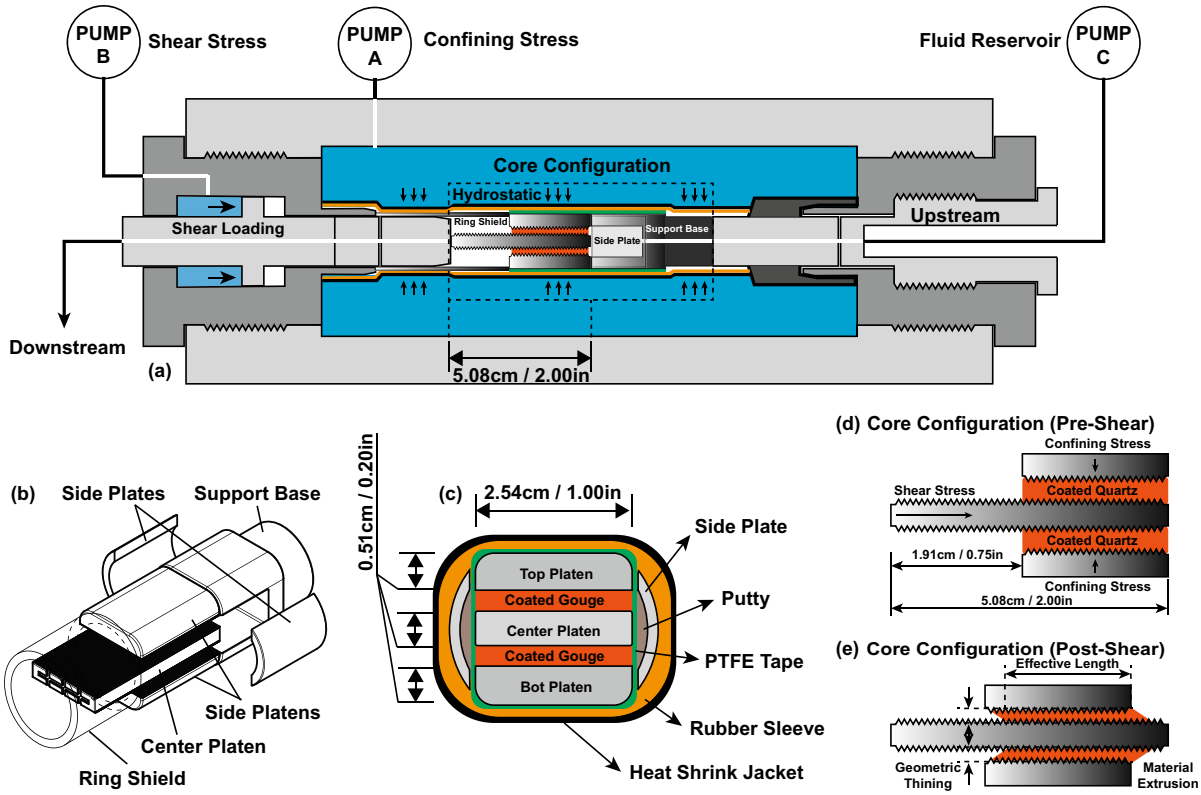

Fig. 1 **a** Schematic of miniature double direct shear apparatus (not-to-scale); **b** 3D exploded-view of the platens (sample gouge, sealing putty, and jacketing system not shown); **c** Cross-section of the sample core, showing the multi-layer hydraulic isolation jacketing system; **d** Side view of the sample core and stress regime, the maximum possible shear displacement is ~ 15 mm (sealing putty and jacketing system not shown); **e** Side-view of the sample core during the test, showing geometric thinning and material extrusion due to gouge extrusion (sealing putty and jacketing system not shown)

through pressure and flow transducers in the precision pumps (Teledyne ISCO) and are recorded by a software interface written in LabVIEW (National Instruments). This DDS configuration also makes highly resolved measurements of friction-permeability on intact rock samples (Im et al. 2018; Im et al. 2017). The sample core (Fig. 1b) is isolated from the confining fluid by multiple jackets (Fig. 1c). In particular, an inner layer of PTFE tape and side putty prevents the pore fluid from pump C leaking out of the sample core. A pair of side protection plates prevent the confining pressure from deforming the inner jacketing covering the side openings of the support base. The assembly is further hydraulically isolated and secured by a rubber sleeve and an outer heat-shrink jacket from confining fluid. Figure 1d shows the detailed stress regime of the sample core. Shear stress is measured by the pressure transducer in pump B, accounting for the effective shear length/area (Fig. 1e) and subtracting the resistance of the system (measured separately without sample core installed). Normal stress is measured by the pressure transducer in pump A, accounting for the same effective area. During the test, gouge materials are extruded out of the sample core due to shearing (Fig. 1e), thus causing geometric thinning, reducing the cross-sectional area for the pore fluid. Note that the extruded materials stay largely immobilized as a plug (Fig. 2e). The geometric thinning effect is approximated by assuming a rectangular extrusion and subtracting the volume of the extruded plug as:

$$\Delta V = h_0 W L \tag{3}$$

in which h_0 is the initial height of the gouge layer, W is the width of the top/bottom platens, L is the shear displacement. This assumption is made due to the technical difficulty of directly measuring the evolution of sample thickness during the experiment. This

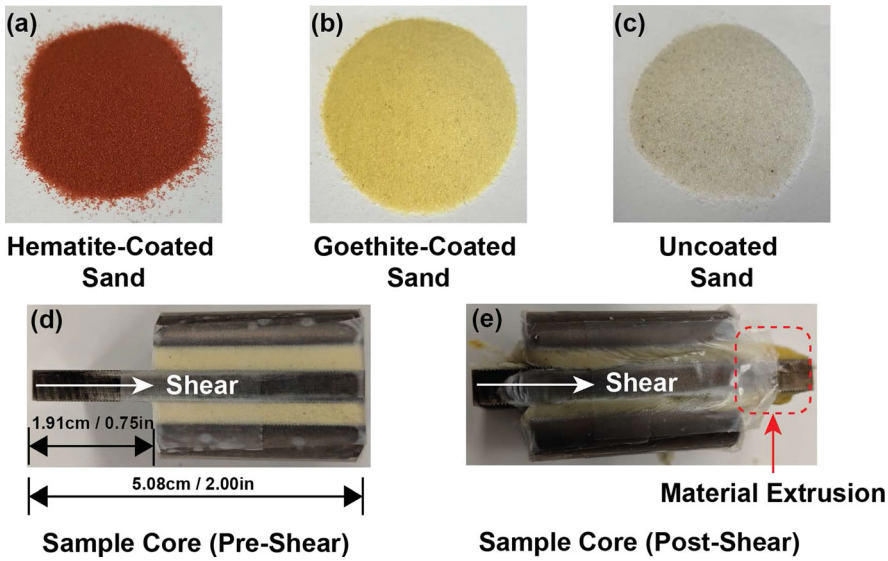

Fig. 2 **a** Hematite-coated sand; **b** Goethite-coated sand; **c** Uncoated US F-110 silica sand; **d** Typical side-view of the sample core with coated-sand (goethite-coated in this case) pre-shear; **e** Typical side-view of the sample core with coated-sand (goethite-coated in this case) post-shear—material extrusion can be observed at the end of the sample core

approach of compensating the geometric thinning effect is exclusively studied and applied in a previous study using a similar setup (Kenigsberg et al. 2019). Darcy's law* is used to evaluate the permeability of the sample:

$$\kappa = \frac{\mu Q L_e}{A \Delta p} \tag{4}$$

*Assuming the fluid is incompressible, the maximum flow rate in all experiments is $\sim$15 ml/min; the corresponding Reynolds number is $\sim$30; the sample is assumed to be quasi-static during experiments.

In which, κ is the shear-parallel permeability; μ is the dynamic viscosity of the pore fluid; Q is the monitored flow rate from pump C; A is the estimated transient cross-section area of fluid flow accounting for geometric thinning; L_e is the effective length of the flow path/shear area; Δp is the hydraulic pressure drop between upstream and downstream (35 kPa in this study).

To further investigate the mechanisms contributing to our observations, we perform scanning electron microscope imaging, and PSD analyses of the iron-oxide coated sands both pre- and post-shear. Pre-shear, iron oxide coated sands are carefully sampled from the prepared stock. Post-shear, sample cores are opened manually, with small portions of the gouge taken from the shear zone and air-dried. Specifically, we use a Helios DualBeam SEM (FEI Company) to take secondary electron reflection images with magnifications ranging from 1000× to 4000×. The operating voltage is 5.0 kV. The PSD analysis of samples is conducted using a Morphologi G3 analyzer (Malvern Panalytical Company), which is capable of characterizing particle sizes ranging from 0.5 microns to several millimeters. The samples are first measured in fixed volume ($\sim$2 mm^3), then dispersed by a short burst of compressed air (0.5 bar fixed pressure) to a circular area (47 mm in diameter) on a clean glass slide, where the sizes of particles are analyzed by the optical scanner.

3.2 Experimental materials

We use US F-110 (US Silica, median particle diameter of $\sim$ 110 μm) fine-grained silica sand as the raw test material (Fig. 2c). The silica sand is coated with hematite and goethite using the "heterogeneous suspension reaction" method (Scheidegger et al. 1993). Iron oxides and corresponding chemicals are purchased from Fisher Scientific. Hematite is purchased in powder form and used as it is. Goethite is synthesized by maturing ferrihydrite (prepared from potassium hydroxide and ferric nitrate, pH 13.6) at 70 °C for 60 h. The goethite chunk mixture is filtrated, air-dried, and ground to fine powders. To synthesize the iron oxide coated sand, the uncoated silica sand is sieved (#200 sieve) to remove fines, pre-washed by 3% hydrogen peroxide solution (H_2O_2) to remove contamination, then air-dried in a vented hood for

24 h. The prepared uncoated sand is mixed and stirred with hematite or goethite powder (weight ratio of 25:1) in sodium nitrate solution ($NaNO_3$, 0.01 M ionic strength) with a controlled pH of 3.0 (achieved by adding nitric acid, HNO_3) for 24 h, resulting in uniformly coated sands (Fig. 2a, b). The coated sand is collected by filtration and then air-dried for 24 h before being stored in containers. SEM images of the hematite-coated sand, pre-shear, show coating particles to be polyhedral in shape with diameters in the sub-micron range. Goethite coatings are fiber-like particles ranging from sub-micron to several microns, featuring a moderate degree of overlap and larger contact area with the host sand grains. Detailed comparison of grain surface texture by SEM and PSD analysis is presented in Sects. 4.4 and 4.5. Figure 2d, e show typical sample cores pre- and post-shear.

3.3 Experimental program

A total of six experiments are conducted for all the samples prepared. All experiments are performed at room temperature. In particular, shear experiments on sample cores with initial sample layer thicknesses of 2 mm or 3 mm (two gouge layers in each sample core as shown in Fig. 2d) are conducted on each of three sample types (hematite-coated, goethite-coated and uncoated). Confining stress is maintained at 3 MPa ($\pm 0.2\%$) with upstream fluid pressure retained at 35 kPa for all tests. For each test, the shear loading is applied according to the following stages:

Stage 1	*Constant Rate Loading* Load at constant shear velocity (10 μm/s) to ~4000 μm shear displacement to reach steady state
Stage 2	*Velocity-Stepping* Step shear velocity between 10 μm/s and 5 μm/s (or 3 μm/s) every 800 μm in shear displacement to capture slip stability behavior, until reaching 9600 μm in total shear displacement
Stage 3	*Slide-Hold-Slide* Reactivate fractures after various hold durations (100 s, 500 s, 800 s, and 1000 s) to determine frictional healing and relaxation

The experimental program is summarized in Table 1, with the results of each test reported, analyzed, and summarized in the following sections.

4 Results

4.1 Evolution of friction

The friction coefficient is calculated as the ratio of shear stress over confining stress. The evolution of the friction coefficient can be interpreted as the evolution of the shear stress under constant confining stress. The evolution of the friction coefficient for the initial sample layer thicknesses of 3 mm and 2 mm are shown in Fig. 3a, b, respectively. Friction evolution curves show a common trajectory in reaching peak shear strength in the first ~ 1000 μm of shear displacement, then declining to a residual strength over the next ~ 1000 μm. Specifically, the hematite-coated sand shows the highest peak shear strength followed by the goethite-coated sand then the uncoated sand, regardless of the difference in initial gouge layer thickness. This comparative order of the peak shear strengths is consistent with previous laboratory observations using similar test materials (Choo et al. 2015; Larrahondo et al. 2011; Larrahondo and Burns 2014). Hematite-coated sand shows a slightly higher residual strength than the rest. All tests exhibit a slight long-term strengthening trend, which is possibly an artifact caused by increasing jacketing resistance beyond a shear offset of ~ 6000 μm. $(a - b)$ values are extracted from stage 2 (velocity stepping, the zoom-in view shown by the insets in Fig. 3a, b). Frictional healing and relaxation are important factors in estimating the energy release for potential seismic hazards, as extracted from the stage 3 (slide-hold-slide).

4.2 Permeability evolution

Permeability evolution for initial sample gouge thicknesses of 3 mm and 2 mm are shown in Fig. 4a, b, respectively. The shear-parallel permeability shares a common trend of increase during the first ~ 2000 μm of shear displacement. Tests uqz-3 mm and uqz-2 mm (uncoated sand with initial gouge layer thickness of 3 mm and 2 mm) reach a plateau at ~ 4000 to 6000 μm in shear displacement—much larger displacement than the hematite- and goethite-coated counterparts. A continuous permeability decrease follows the plateaus in all tests. Tests uqz-3 mm, uqz-2 mm, and hqz-2 mm show a sharp decline in permeability while tests gqz-3 mm and gqz-2 mm

Table 1 Experimental program

Test	Experiment material	Initial sample thickness (mm)	Velocity step (μm/s)	Hold-slide-hold duration (s)
uqz-2mm	Uncoated sand	2	10/5/10/5/3/5/10	100/500/800/1000
uqz-3mm	Uncoated sand	3	10/5/10/5/3/5/10	100/500/800/1000
hqz-2mm	Hematite coated sand	2	10/5/10/5/3/5/10	100/500/800/1000
hqz-3mm	Hematite coated sand	3	10/5/10/5/*/5/10	100/500/800/1000
gqz-2mm	Goethite coated sand	2	10/5/10/5/3/5/10	100/500/800/1000
gqz-3mm	Goethite coated sand	3	10/5/10/5/3/5/10	100/500/800/1000

*Pump issue resulted in failure to achieve this corresponding velocity step. A hold step is performed instead

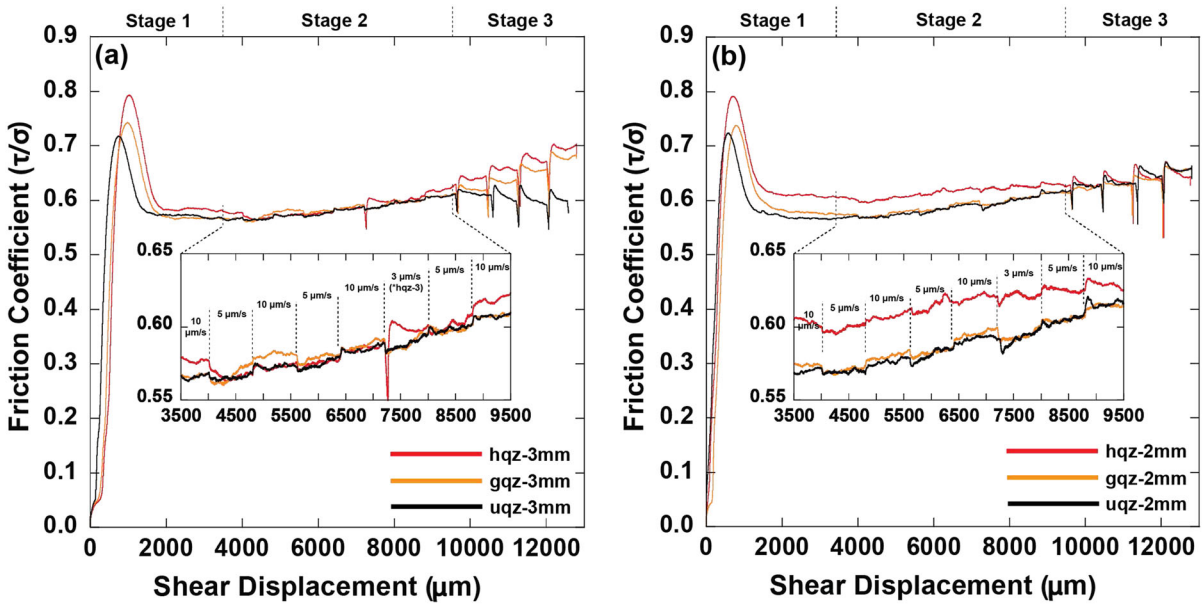

Fig. 3 **a** Friction evolution of hematite-coated, goethite-coated, and uncoated sand with initial sample gouge layer thickness of 3 mm. Inset shows a zoom-in view of the velocity-stepping stages for each experiment. One of the velocity steps in test hqz-3 mm is replaced by a hold due to a pump issue. **b** Friction evolution of hematite-coated, goethite-coated, and uncoated sand with initial sample gouge layer thickness of 2 mm. Inset shows the zoom-in view of the velocity-stepping stages for each experiment

show moderate permeability decline. Test hqz-3 mm shows the smallest overall permeability. No systematic trends in permeability are observed during the velocity-stepping stages for all tests.

At the slide-hold-slide stage, the permeability increases with each hold and decreases with each slide. Specifically, during holds (Stage 3, slide-hold-slide), a gradual permeability increase is observed. A representative example is shown in Fig. 5a, b. Specifically, Fig. 5a shows permeability vs. shear displacement, and Fig. 5b shows the same permeability window vs. time. Permeability increases gradually with time during holds but decreases rapidly during shear-reactivation, which is different from previous observations of permeability decline due to fault sealing (Im et al. 2018; Elkhoury et al. 2006). Detailed discussion is provided in Sect. 5.2.

4.3 Frictional stability, healing, and relaxation

$(a - b)$ values, frictional healing rate, and relaxation rate are among the most important stability parameters

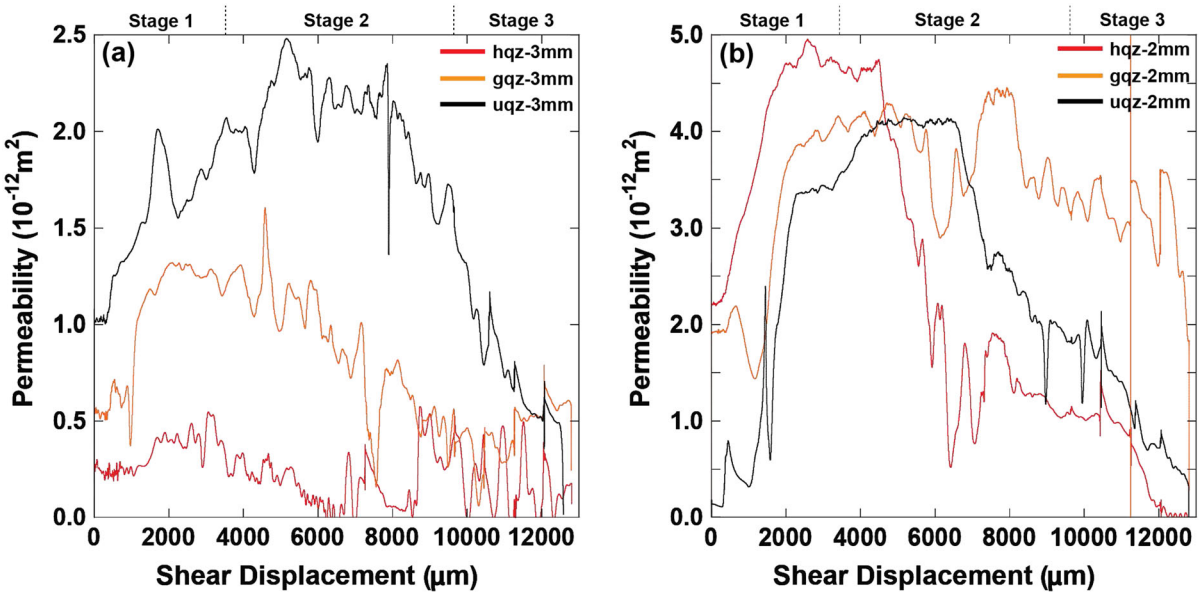

Fig. 4 Permeability evolution of samples with **a** 3 mm, then **b** 2 mm initial gouge layer thickness

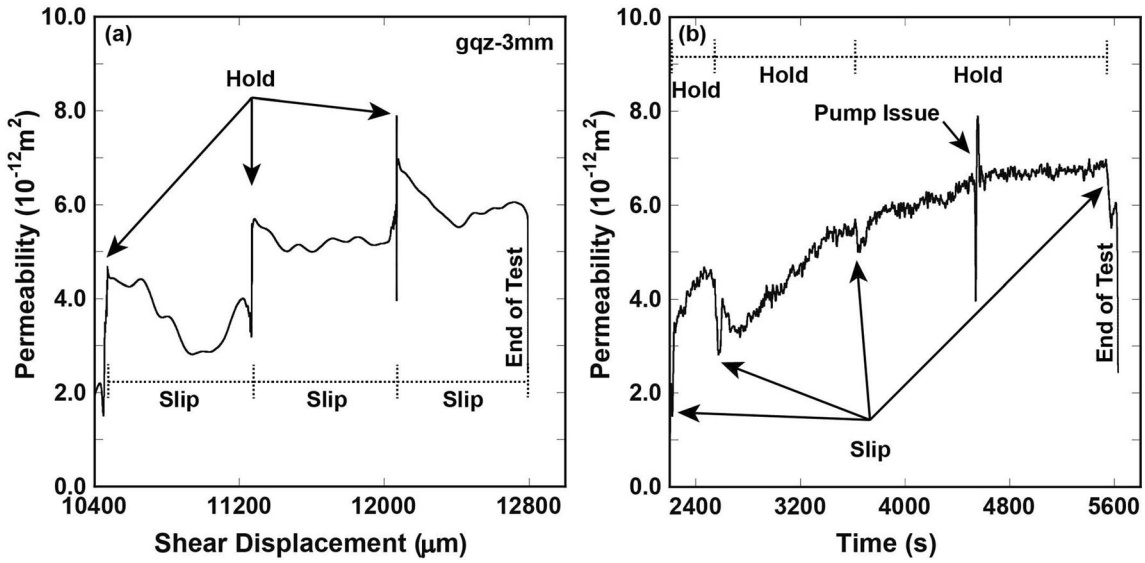

Fig. 5 **a** Zoomed-in view of permeability evolution (gqz-3 mm) vs. displacement; **b** Permeability evolution (gqz-3 mm) vs. time

which determine the potential-for, and style-of, reactivation of faults. $(a - b)$ values are obtained from the friction evolution during each velocity step (Stage 2; velocity stepping, typically from ~ 4000 to ~ 9600 μm in shear displacement, insets in Fig. 3). In all the tests, a global long-term strengthening trend is observed, possibly caused by increasing resistance of the jacketing system beyond a shear offset of ~ 6000 μm. In our analysis, $(a - b)$ values are calculated for each velocity step. We assume the global strengthening trend is linear within each velocity step window. A typical pattern of friction evolution with a velocity step is shown in Fig. 6a. The global strengthening trend is removed by subtracting

the linear deviation estimated from the start and end of the window (black line). The $(a - b)$ values are calculated as:

$$(a - b) = \frac{\mu_1 - \mu_0}{\ln\left(\frac{V_1}{V_0}\right)} \quad (5)$$

in which μ_0 and μ_1 are the steady-state friction coefficients before and after the velocity step. The values are calculated by averaging friction coefficients at the beginning and the end of the chosen window, respectively; V_0 and V_1 are the steady-state shear velocities before and after the velocity step. The $(a - b)$values for each type of sample and corresponding statistics (mean values and standard deviations) are summarized in Fig. 6b. The standard deviation error bar shows that hematite-coated sand can feature negative $(a - b)$ values, indicating potential velocity-weakening behavior. Conversely, goethite-coated sand and uncoated sand show positive $(a - b)$ values, statistically suggesting mostly velocity-strengthening behavior. It is worth noting that uncoated sand features a wide range of $(a - b)$ values.

We estimate frictional healing rates and stress relaxation rates through repeated slide-hold-slide stages (typically from ~ 9600 μm to 12,500 μm in shear displacement). Specifically, we performed four holds of different durations during each test. The inset of Fig. 7a shows a conceptual slide-hold-slide cycle. Frictional healing and relaxation are evaluated for each hold as $\Delta\mu_s$ and $\Delta\mu_r$ and plotted against hold duration. Frictional healing rate and relaxation rate are calculated as the slope of $\Delta\mu_s$ and $\Delta\mu_r$ over the hold time duration, respectively. The frictional healing rate defines how rapidly the sample evolves to peak friction after reinitiating sliding from the prior steady-state friction (before the previous hold). Relaxation rate is defined as the decrease in friction per unit time during holds. The results of frictional healing rate and relaxation rate are summarized in Fig. 7a, b with fitted slopes, indicating the long-term trajectory of healing and relaxation. Goethite-coated sand shows the highest slope (0.013, slope calculated against logarithmic time), which is almost double that for hematite-coated sand (0.007). Uncoated sand shows a similar slope for frictional healing rate as the goethite-coated sand (0.012). Goethite-coated sand also features the highest relaxation rate slope (0.056) followed by hematite-coated sand (0.048), then uncoated sand (0.031). These observations indicate that goethite coatings increase both frictional healing and relaxation, while hematite coatings increase relaxation but decrease the frictional healing compared to uncoated sand.

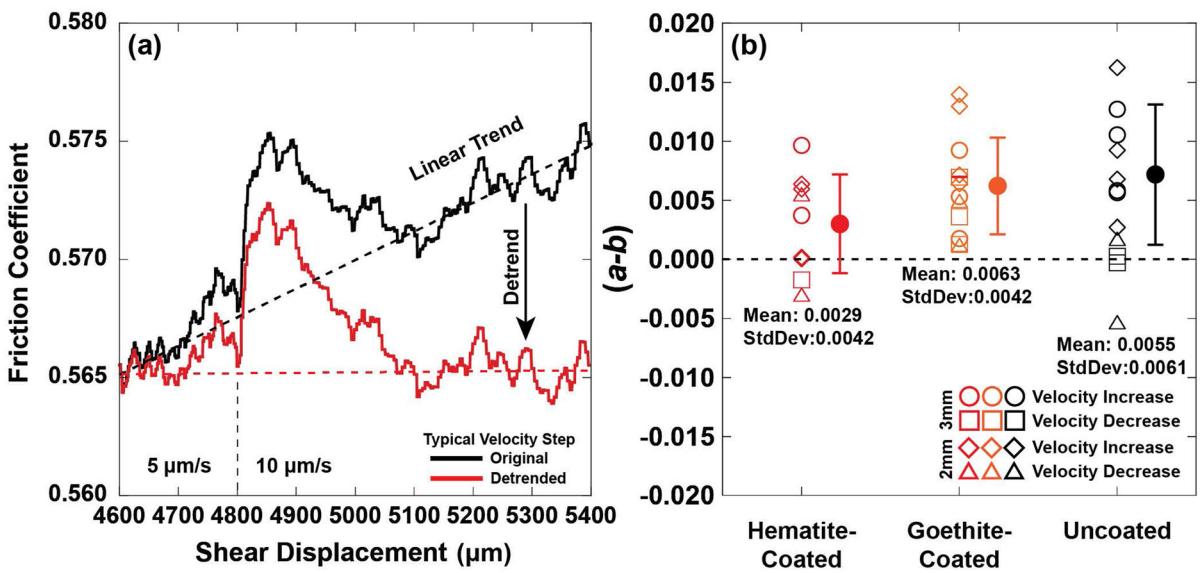

Fig. 6 **a** Typical frictional evolution at a velocity step from test Stage 2 (velocity-stepping). The global strengthening trend is linearly removed for the analysis of $(a - b)$; **b** Statistical summary of $(a - b)$ values obtained from all velocity steps

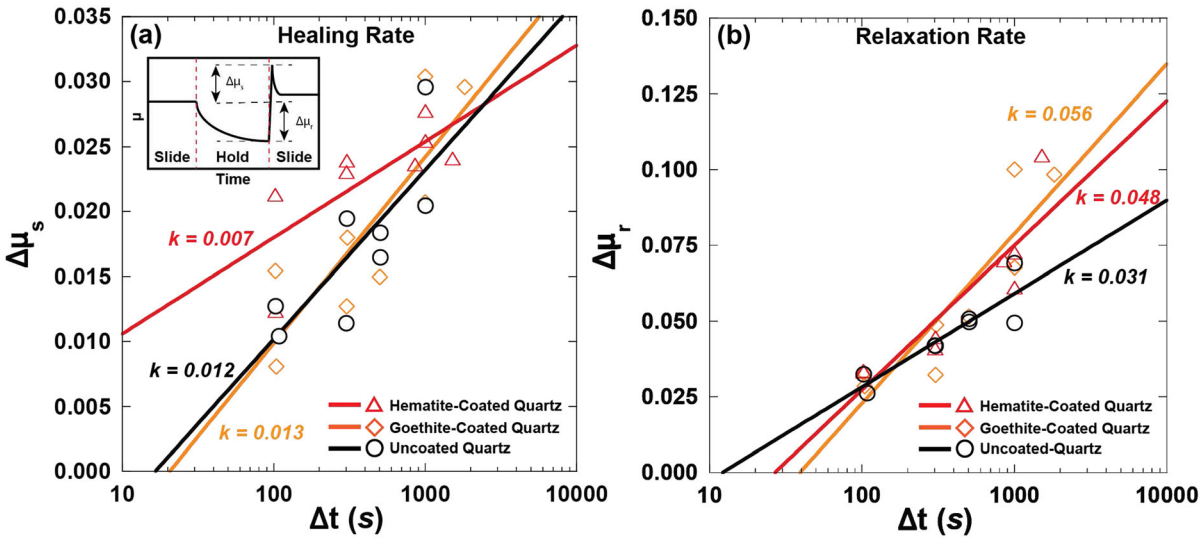

Fig. 7 **a** Frictional healing rate and fitted slope (slope calculated against logarithmic time) for each sample type. Inset shows a typical conceptual slide-hold-slide cycle. **b** Frictional relaxation rates and linearly fitted slope (slope calculated against logarithmic time) for each sample type

4.4 SEM analysis

Typical SEM images of grain-coating microstructures are shown in Fig. 8. SEM images of the hematite-coated sand, pre-shear, show coating particles to be polyhedral in shape and scattered on the sand grain surface (Fig. 8a), with individual coating particle diameters in the sub-micron range. Conversely, the image of goethite-coated sand, pre-shear, shows fiber-like coating particles ranging from sub-micron to several microns, featuring a moderate degree of overlap and larger contact area with the host grains (Fig. 8b). Figure 8c, d are SEM images of the hematite- and goethite-coated sand grains post-shear. Figure 8c shows wear products from grain damage (chips and fragments of silica sand) and highly concentrated clusters containing hundreds of hematite particles on the surface of the grain. Figure 8d shows a clean surface, which is likely the result of grain damage during shearing. Interestingly, no goethite is present on this surface. Further discussion is provided in Sect. 5.1.

4.5 Particle size distribution analysis

In addition to the SEM images, particle size distributions (PSD) are recovered for the hematite- and goethite-coated samples, both pre- and post-shear. The PSD results of particle number percentages vs. particle size of two batches of samples are summarized in Fig. 9. In general, hematite-coated sand shows significantly more particles in total than the goethite-coated sand. The hematite-coated sand shows a slight increase in the percentage of sub-micron particles after shear (Fig. 9a, c). The total number of particles is reduced (insets of Fig. 9a, c). Conversely, the PSD of goethite-coated sand shows a decrease in the percentage of sub-micron particles and an increase in the proportion of particles with sizes larger than 1 μm (Fig. 9b, d). The total number of particles in the goethite-coated sand increases post-shear (insets of Fig. 9b, d). Further discussion is provided in Sect. 5.2.

5 Discussion

5.1 Implications from SEM and PSD analysis

SEM images show that coating materials, both hematite, and goethite, increase the complexity of the surface texture of the host sand grains. Therefore, it is likely that such textural complexity contributes to the observed increase in the overall frictional resistance of the coated sands, resulting in higher peak frictional strength relative to uncoated sands. Additionally, goethite is mechanically weaker than

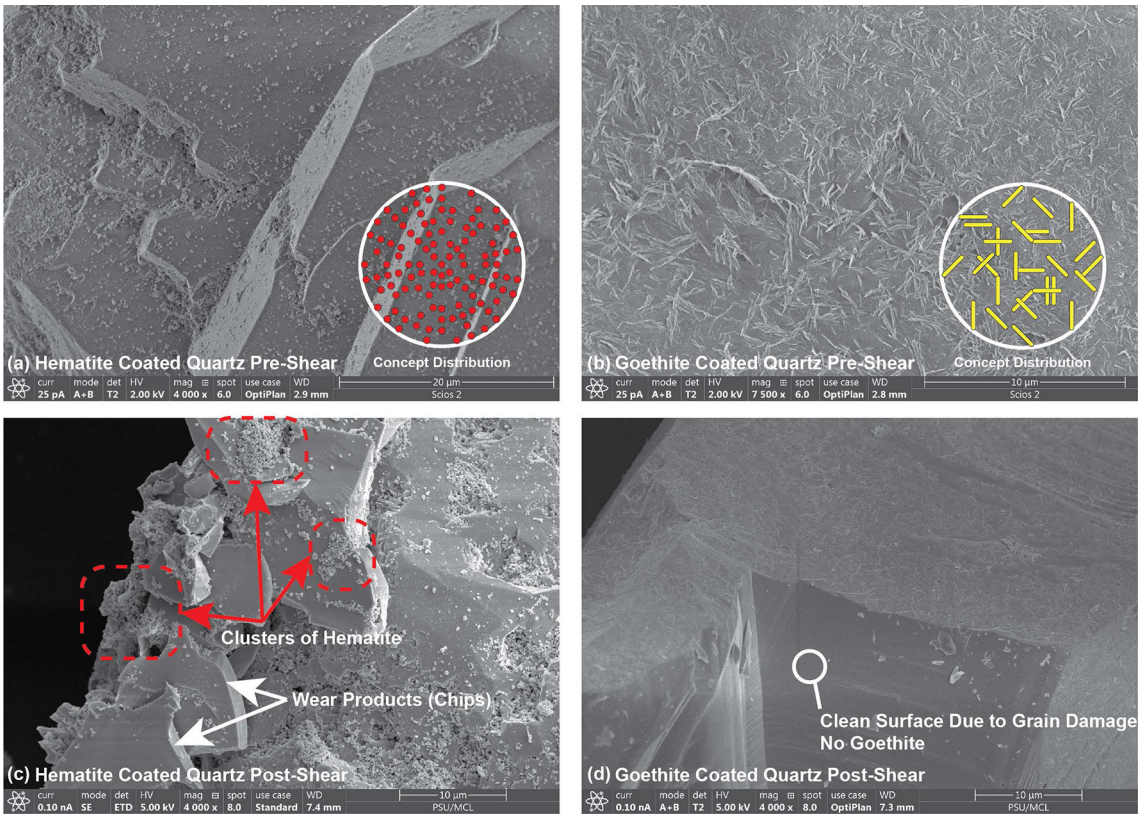

Fig. 8 **a** Typical SEM image of hematite-coated sand pre-shear. Inset shows a conceptual distribution; **b** Typical SEM image of goethite-coated sand pre-shear. Inset shows a conceptual distribution; **c** Hematite-coated sand post-shear. Wear products, and coating particle clusters are highlighted; **d** Goethite-coated sand post-shear. Grain damage surface is clean and free of goethite coating

hematite - this may help reconcile why goethite-coated sand returns a lower peak strength than hematite-coated sand. Due to the lack of complex grain texture provided by the coating materials, the uncoated sand shows the lowest peak shear strength. After reaching the steady state, except for the hematite-coated sand, the residual strength of the goethite-coated sand approaches that of the uncoated sand. Although the precise reason is unclear, a possible explanation is that goethite coating, while strongly attached to the host grain, does little to impact residual strength than the hematite coated particles. The latter can be transported and deposited/clustered by mechanical and fluid interaction, introducing more drastic changes to the grain surface roughness and thereby contributing to the slightly higher residual strength.

Large hematite coating clusters and wear products (chips and fragments of quartz, white arrows in Fig. 8c) are commonly observed on the hematite-coated sand grains, post-shear. The origins of these wear products and clusters are speculated to be due to coupled fluid-shear interactions with coating particles, in which wear products and coating materials are liberated, transported, and deposited in clusters by the fluid. Wear products are also present in the post-shear goethite-coated sands, but no drastic change is observed in terms of the form and distribution of the goethite coating particles. The vacant substrate surface, as shown in Fig. 8d, is plausibly caused by grain damage during shearing. However, no deposition of goethite coating particles is present on the surface. This is evidence that goethite particles exhibit a stronger attachment to the host grain and are thus less susceptible to fluid liberation and transport. These observations imply that hematite coatings are more readily transportable by fluid than the goethite coatings.

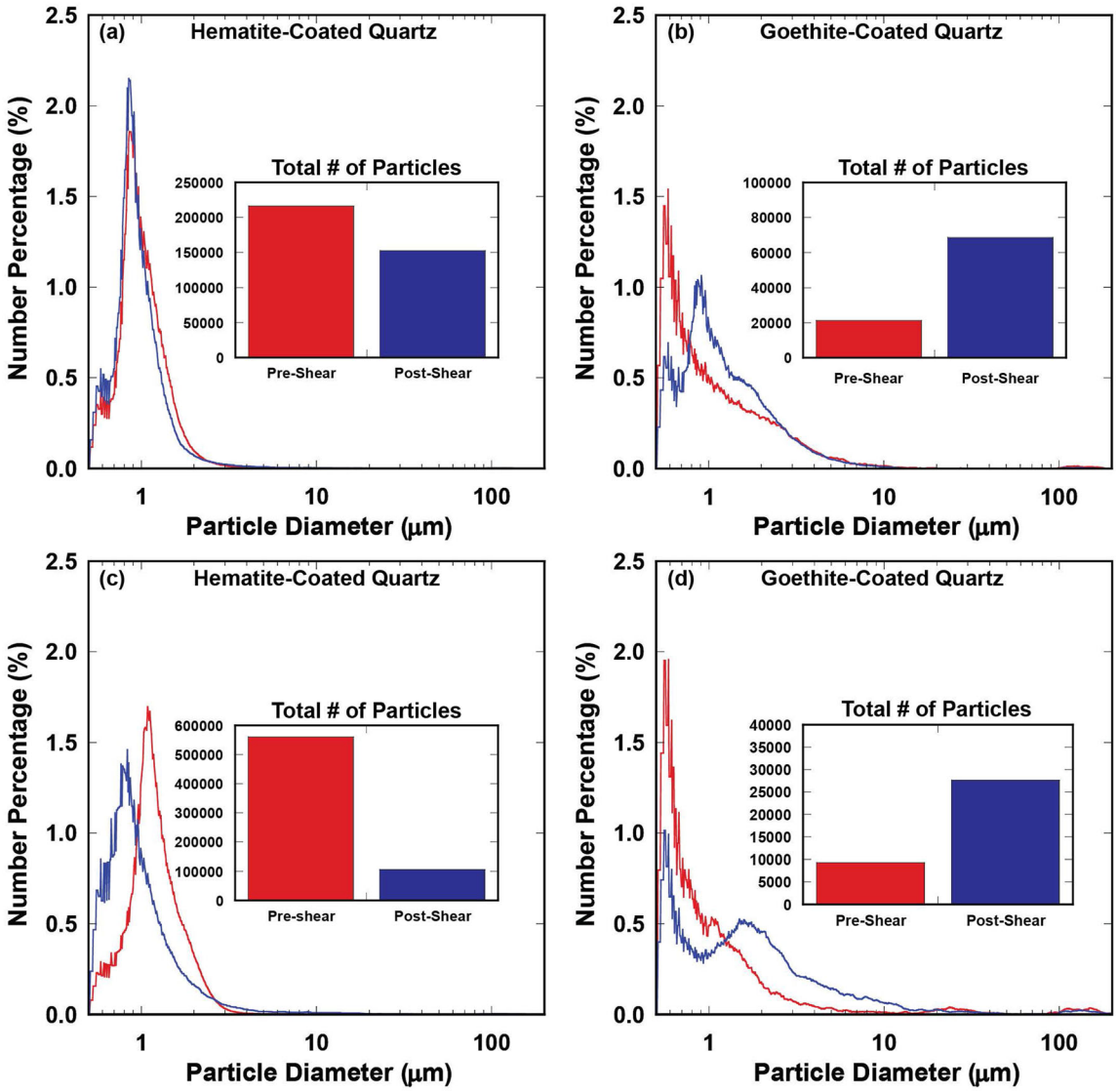

Fig. 9 **a** Particle size distribution analysis of hematite-coated sand both pre- and post-shear, first batch; **b** Goethite-coated sand, first batch; **c** Hematite-coated sand, second batch; **d** Goethite-coated sand, second batch

5.2 Mechanisms for permeability evolution

Experimental results show that shear-parallel evolution of permeability features general trends of an increase to a peak permeability and then a decrease. This trend can be explained by the initial dominance of shear dilation being gradually replaced by the dominance of shear compaction. Moreover, the overall small (Fig. 4a) and sharp decline of permeability in hematite-coated sand (Fig. 4b) is possibly related to the liberation, transport, and clogging of the coating particles and shear-generated wear products.

It is well known that the permeability of a porous medium is closely related to structural dilation, compaction, and the resulting evolution of the pore network. Test results show that the shear-parallel permeability of hematite-coated sand is lower than that of goethite-coated sand. Specifically, hqz-2 mm shows a sharp decrease in permeability after peaking at the plateau. Given that the application of contrasting

coating materials is the only variable in our experiments, this sharp decline in permeability can only be attributed to the strong effect of the clustering of coatings and clogging of the connecting throats in the pore network. The PSD analysis also implies this mechanism. Specifically, the clustering of the coating particles due to fluid transport reduces the total number of particles because the clustered particles are regarded as a part of a host grain. While wear-product generation involves contact grinding, which creates micron-sized chips from the skin of intact sand grains, thus increasing the total number of particles. Wear product generation occurs in both hematite- and goethite-coated quartz during shearing. In the case of hematite-coated quartz, the coating particles are more easily librated, transported, and relocated as clusters adhering to host grains by the fluid - which has a more significant impact than the concurrent generation of wear products. The result is a reduced total number of particles post-shear. Conversely, for the goethite-coated quartz, the coating particles seldom migrate with the fluid, as suggested by Fig. 8d. Thus the generation of wear products dominates, increasing the total number of particles, post-shear. Consideration of this competition between the two processes helps reconcile the difference between the different permeability evolution trends apparent for the hematite- versus the goethite-coated sand. Permeability decrease by wear product clogging is likely to be enhanced when combined with the coating clustering effect, as suggested by the sharp permeability decline in hematite-coated sand after reaching its peak.

Increases in permeability are observed during the hold periods, as shown in Fig. 5. This contradicts observations previously reported in the existing literature (Im et al. 2018) but is consistent with recent laboratory findings under a similar experimental setup and conditions (Madara 2018). The possible explanation for our observation is that the confining stress in our tests is relatively low compared to the existing studies that focus on faults with long-term consolidation and large confining stresses. Permeability is usually governed by the presence of major fluid channels, which can be readily altered by the combined effects of shearing, fluid mobilization of particles, and corresponding clogging effects. The permeability enhancement observed during holds in our tests can be attributed to the maturation of major fluid channels during holds. Slip reactivation, following a hold, introduces strong shear compaction, destroying the established major fluid channels from the previous hold and causing a permeability decrease. The permeability evolution cycle repeats with the next hold.

6 Conclusions

We report observations and analysis of the influence of hematite and goethite coatings on the shear strength, frictional stability, and permeability evolution of sands using a novel miniature double direct shear (DDS) apparatus. The laboratory conditions approximate the response of sandstone faults under shearing and with fluid flow. The hematite- and goethite-coated sand samples are synthesized in the laboratory as analog pristine (hematite-coated) and CO_2-transformed (goethite-coated) gouge materials. The laboratory results and analyses can be used as a reference to predict the behavior of faults in sandstone that are subjected to CO_2 bleaching resulting from CO_2 migration from a deeper storage reservoir. Our results and analyses from the experiments suggest the following conclusions:

1. Hematite and goethite coatings increase the frictional strength of the sand. The goethite-coated sand is slightly weaker than hematite-coated sand with regard to peak strength.
2. Goethite-coated sands (CO_2-transformed) show velocity-strengthening behavior while featuring higher frictional healing and relaxation to that of the hematite-coated materials. This suggests that CO_2 altered sandstones may feature a reduced risk of seismic hazard.
3. Goethite-coated sands (CO_2-transformed) feature larger overall permeability than hematite-coated sands (pristine), which suggests a higher risk of accelerated migration, breaching, and loss of fluid inventory.
4. SEM and PSD analysis of samples, both pre- and post-shear, imply that hematite coatings can be readily liberated, transported, and relocated as clusters on sand grains, resulting from fluid interactions. This can significantly alter the transport characteristics of the porous medium.

This study provides insights into how hematite (pristine, unaltered) and goethite coatings (CO_2-transformed) can influence shear strength, stability, and permeability of faults in sandstone. However, our experimental results are limited in the variations of confining stresses and temperature. Future investigations, potentially long-term reactive shear-flow experiments with different confining stresses and temperatures, on samples with various mineral compositions are necessary to strengthen these conclusions.

Acknowledgements This work is a partial result of the support provided by DOE Grant DE-FE0023354 and NSF Grant EAR-1552211. This support is gratefully acknowledged. Especially appreciated is the support of Dr. Peter Heaney and Si Athena Chen in the production of the iron oxides used in the experiments.

Author contributions The corresponding author of this manuscript, Chaoyi Wang, performed the synthesis of hematite- and goethite-coated sand sample, conducted the shear-flow experiments, analyzed test data, and wrote the main text of the manuscript. The second author, Prof. Derek Elsworth, provided significant and necessary guidance and insights for this study, and contributed greatly to the editing of the main text. All authors have reviewed the manuscript before submission.

Compliance with ethical standards

Competing interest The authors declare no competing interests.

References

Altman SJ et al (2014) Chemical and hydrodynamic mechanisms for long-term geological carbon storage. J Phys Chem C 118:15103–15113

Bader AG et al (2014) CO_2 storage capacity evaluation in deep saline aquifers for an industrial pilot selection Methodology and results of the France Nord project. Energy Proc. https://doi.org/10.1016/j.egypro.2014.11.300

Bakker E, Hangx SJT, Niemeijer AR, Spiers CJ (2016) Frictional behaviour and transport properties of simulated fault gouges derived from a natural CO_2 reservoir. Int J Greenh Gas Control 54:70–83

Benson SM, Cole DR (2008) CO_2 sequestration in deep sedimentary formations. Elements 4:325–331

Busch A, Müller N (2011) Determining CO_2/brine relative permeability and capillary threshold pressures for reservoir rocks and caprocks: recommendations for development of standard laboratory protocols. Energy Proc. https://doi.org/10.1016/j.egypro.2011.02.610

Busch A et al (2014) The green river natural analogue as a field laboratory to study the long-term fate of CO_2 in the subsurface. Energy Proc. https://doi.org/10.1016/j.egypro.2014.11.304

Choo H, Larrahondo J, Burns SE (2015) Coating effects of nano-sized particles onto sand surfaces: small strain stiffness and contact mode of iron oxide-coated sands. J Geotech Geoenviron Eng 141:04014077

Collettini C, Niemeijer A, Viti C, Marone C (2009) Fault zone fabric and fault weakness. Nature 462:907–910

Crawford BR, Faulkner DR, Rutter EH (2008) Strength, porosity, and permeability development during hydrostatic and shear loading of synthetic quartz-clay fault gouge. J Geophys Res Solid Earth 113:1–14

Cundy AB, Hopkinson L (2005) Electrokinetic iron pan generation in unconsolidated sediments: implications for contaminated land remediation and soil engineering. Appl Geochem 20:841–848

De Lary L et al (2015) Quantitative risk assessment in the early stages of a CO_2 geological storage project: implementation of a practical approach in an uncertain context. Greenh Gases Sci Technol. https://doi.org/10.1002/ghg.1447

Dieterich JH (1978) Time-dependent friction and the mechanics of stick-slip. Pure Appl Geophys Pageoph 116:790–806

Dieterich JH (1979a) Modeling of rock friction 2. Simulation of preseismic slip. J Geophys Res Solid Earth 84:2169–2175

Dieterich JH (1979b) Modeling of rock friction 1. Experimental results and constitutive equations. J Geophys Res Solid Earth 84:2161–2168

Elkhoury JE, Brodsky EE, Agnew DC (2006) Seismic waves increase permeability. Nature 441:1135–1138

Ellsworth WL (2013) Injection-induced earthquakes (80-). Science 341:1–8

Elsworth D, Spiers CJ, Niemeijer AR (2016) Understanding induced seismicity. Science 354:1380–1381

Fabriol H et al (2010) The Géocarbone-Monitoring project: main results and recommendations for monitoring deep geological CO_2 storage in the Paris Basin. Oil Gas Sci. Technol. https://doi.org/10.2516/ogst/2010003

Fang Y, Wang C, Elsworth D, Ishibashi T (2016) Friction-permeability relationships for reservoir caprocks. In: 50th US rock mechanics/geomechanics symposium, 2016 vol 3, pp 2388–2397

Fang Y, Wang C, Elsworth D, Ishibashi T (2017) Seismicity-permeability coupling in the behavior of gas shales, CO_2 storage and deep geothermal energy. Geomech Geophys Geo-Energy Geo-Resour 3:189–198

Fang Y, Elsworth D, Wang C, Jia Y (2018) Mineralogical controls on frictional strength, stability, and shear permeability evolution of fractures. J. Geophys. Res. Solid Earth 123:3549–3563

Fleury M et al (2011) Evaluating sealing efficiency of caprocks for CO_2 storage: an overview of the geocarbone integrity program and results. Energy Proc. https://doi.org/10.1016/j.egypro.2011.02.501

Guglielmi Y, Cappa F, Avouac JP, Henry P, Elsworth D (2015) Seismicity triggered by fluid injection-induced aseismic slip (80-). Science 348:1224–1226

Hangx S, Bakker E, Bertier P, Nover G, Busch A (2015) Chemical-mechanical coupling observed for depleted oil reservoirs subjected to long-term CO_2-exposure—a case

study of the Werkendam natural CO_2 analogue field. Earth Planet Sci Lett. https://doi.org/10.1016/j.epsl.2015.07.044
Ikari MJ, Marone C, Saffer DM (2011) On the relation between fault strength and frictional stability. Geology 39:83–86
Im K, Elsworth D, Marone C, Leeman J (2017) The impact of frictional healing on stick-slip recurrence interval and stress drop: implications for earthquake scaling. J Geophys Res Solid Earth 122:10102–10117
Im K, Elsworth D, Fang Y (2018) The influence of preslip sealing on the permeability evolution of fractures and faults. Geophys Res Lett 45:166–175
Kampman N et al (2013) Scientific drilling and downhole fluid sampling of a natural CO_2 reservoir. Sci Drill. https://doi.org/10.5194/sd-16-33-2013
Kampman N et al (2014) Drilling and sampling a natural CO_2 reservoir: implications for fluid flow and CO_2-fluid-rock reactions during CO_2 migration through the overburden. Chem Geol. https://doi.org/10.1016/j.chemgeo.2013.11.015
Kenigsberg AR, Rivière J, Marone C, Saffer DM (2019) The effects of shear strain, fabric, and porosity evolution on elastic and mechanical properties of clay-rich fault gouge. J Geophys Res Solid Earth 124:10968–10982
Larrahondo JM, Burns SE (2014) Laboratory-prepared iron oxide coatings on sands: surface characterization and strength parameters. J Geotech Geoenviron Eng 140:04013052
Larrahondo JM, Choo H, Burns SE (2011) Laboratory-prepared iron oxide coatings on sands: submicron-scale small-strain stiffness. Eng Geol 121:7–17
Li Z, Elsworth D, Wang C, Im K (2019) A new apparatus for the concurrent measurement of friction and permeability evolution in fault gouge. Int J Rock Mech Min Sci 121:104046
Madara BJ (2018) Laboratory studies of permeability evolution: roles of fracture, shear, dynamic stressing, and reservoir rock properties (Pennsylvania State University)
Mair K, Marone C (1999) Friction of simulated fault gouge for a wide range of velocities and normal stresses. J. Geophys. Res. Solid Earth 104:28899–28914
Major JR et al (2014) The effect of CO_2-related diagenesis on geomechanical failure parameters: fracture testing of CO_2-altered reservoir and seal rocks from a natural analog at Crystal Geyser, Utah. In: 48th US rock mechanics/geomechanics symposium 2014, vol 1, pp 176–180
Marone C (1998a) Laboratory-derived friction laws and their application to seismic faulting. Annu Rev Earth Planet Sci 26:643–696
Marone C (1998b) The effect of loading rate on static friction and the rate of fault healing during the earthquake cycle. Nature 391:69–72
Rao SM, Sridharan A, Ramanath KP (1995) Collapse behavior of an artificially cemented clayey silt. Geotech Test J 18:334–341
Rice JR, Lapusta N, Ranjith K (2001) Rate and state dependent friction and the stability of sliding between elastically deformable solids. J Mech Phys Solids 49:1865–1898
Rinehart AJ, Dewers TA, Broome ST, Eichhubl P (2016) Effects of CO_2 on mechanical variability and constitutive behavior of the lower tuscaloosa formation, cranfield injection site, USA. Int J Greenh Gas Control 53:305–318
Rohmer J, Seyedi DM (2010) Coupled large scale hydromechanical modelling for caprock failure risk assessment of CO_2 storage in deep saline aquifers. Technol Rev l'Institut Français du Pétrole, Oil Gas Sci. https://doi.org/10.2516/ogst/2009049
Ruina A (1983) Slip instability and state variable friction laws. J Geophys Res 88:10359–10370
Samuelson J, Spiers CJ (2012) Fault friction and slip stability not affected by CO_2 storage: evidence from short-term laboratory experiments on North Sea reservoir sandstones and caprocks. Int J Greenh Gas Control 11:78–90
Samuelson J, Elsworth D, Marone C (2009) Shear-induced dilatancy of fluid-saturated faults: experiment and theory. J Geophys Res Solid Earth 114:1–15
Scheidegger A, Borkovec M, Sticher H (1993) Coating of silica sand with goethite: preparation and analytical identification. Geoderma 58:43–65
Scholz CH (1998) Earthquakes and friction laws. Nature 391:37–42
Schwertmann U (1971) Transformation of hematite to goethite in soils [4]. Nature 232:624–625
Schwertmann RMC (2003) The iron oxides: structure, properties, reactions, occurences and uses, 2nd edn. Wiley, New York
Wang C, Elsworth D, Fang Y, Liu K, Jia Y (2017a) Weakening effects of microstructural tribological films in CO_2-altered reservoirs and caprocks. In: 51st U.S. rock mechanics/geomechanics symposium, vol 2, pp 1047–1054
Wang C, Elsworth D, Fang Y (2017b) Influence of weakening minerals on ensemble strength and slip stability of faults. J Geophys Res Solid Earth 122:7090–7110
Yasuhara H et al (2006) Evolution of fracture permeability through fluid-rock reaction under hydrothermal conditions. Earth Planet. Sci. Lett. 244:186–200
Zoback MD, Gorelick SM (2012) Earthquake triggering and large-scale geologic storage of carbon dioxide. Proc Natl Acad Sci USA 109:10164–10168

Publisher's Note Springer Nature remains neutral with regard to jurisdictional claims in published maps and institutional affiliations.